AM1.5G solar radiation, which is commonly used in photovoltaic device characterization, mimics the radiation of the sun. It is important to calculate the enhancement factors under AM1.5G to identify the contribution of plasmonic architecture. The overall absorption is given by the average of absorptivity under both TE- and TM-polarized illumination, i.e., (ATM + ATE)/2. We compute the performance enhancement of the plasmonic solar cell architecture (in %) under AM1.5G solar radiation by using Eq. (3).

$$\frac{\int_{400nm}^{800nm} (\frac{A_{TM}(\lambda) + A_{TE}(\lambda)}{2}) \times AM1.5G(\lambda)d\lambda - \int_{400nm}^{800nm} A_{bare}(\lambda) \times AM1.5G(\lambda)d\lambda}{\int_{400nm}^{800nm} A_{bare}(\lambda) \times AM1.5G(\lambda)d\lambda} \times 100 \quad (3)$$

3. Simulation Results, Analyses and Discussion

The first investigated plasmonic architecture is the bottom grating architecture. This structure consists of periodic gratings placed on top of the cathode layer. The cross-sectional view of the corresponding plasmonic architecture is presented in Fig. 1(b). In this architecture, some of the active material is replaced by the metallic grating. We do not add any active material here to compensate for the removed active material; the active material thickness is fixed to 100 nm in all cases. The second plasmonic architecture, which we considered for comparison purposes, is the top grating embedded in the organic solar cell device, as shown in Fig. 1(c). In this architecture, the hole transport layer (PEDOT:PSS layer) is partially substituted by the periodic grating. Such a top periodic grating structure has been widely studied in the previous literature [4,9,12,13,17–19,29]. Here we simulate and compare our proposed plasmonic architecture of patterned backcontact with this well-studied top grating architecture to identify the performance enhancement contribution of our plasmonic architecture located on the bottom.
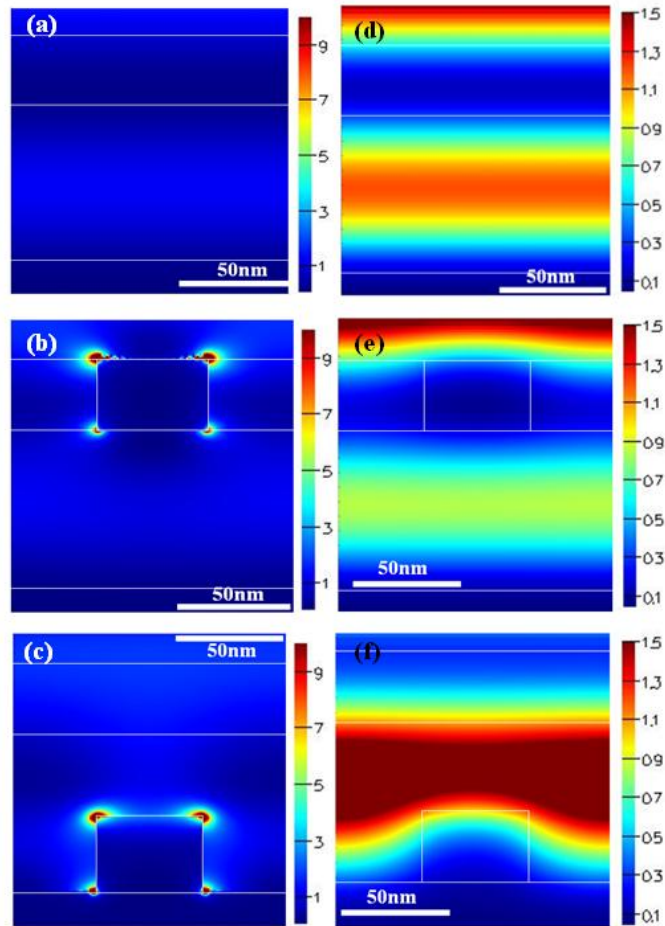
Fig. 2. Electric field ($|E|^2$) maps at $\lambda = 600$ nm under TM illumination for (a) the bare (reference) structure consisting of glass/ITO/PEDOT:PSS/P3HT:PCBM/Ag, (b) the top grating structure – partially substituting the PEDOT:PSS layer with Ag periodic gratings, and (c) the Ag bottom grating case – adding periodic grating on top of backcontact – and under TE illumination for (d) the bare, (e) the top grating, and (f) the bottom grating structure for parameters of P = 130 nm, LT1 = 150 nm, LT2 = 50 nm, LT3 = 100 nm, w1 = 50 nm, w2 = 50 nm and h = 50 nm. Here one unit cell of the repeating grating structure is used to visualize the electric field maps.

Figure 2(a) shows the field profiles generated in the bare (non-metallic) architecture under TM-polarized illumination. The field intensity in the volume of the active material is slightly higher compared to other layers. Figure 2(b) presents the electric field map of the top grating architecture under TM-polarized at $\lambda = 600$ nm. We observe in Fig. 3(a) that the absorptivity performance of the top grating based architecture is lower than that of the bare architecture. The field profiles show that the top metallic gratings reflect the incoming light, and this reflection causes a decrease in the absorption of the active material. Figure 2(c) clearly proves the surface plasmons generated around the bottom metallic gratings (represented as high field intensities in the color map), which are localized in the active material. The opposite surface of the grating applies an effective restoring force on the present free electrons in the metal. Therefore, a resonance that leads to a field localization can form around the corners of the metallic grating. The localized surface plasmons that are non-propagating excitations of the conduction electrons of the metallic structure are observed around the bottom metallic grating. This localized surface plasmon mode concentrated in the silver grating/organic absorbing

material interface increases the absorptivity of the active materials since the absorptivity is linearly proportional to the intensity (electric field square) in the volume of the active material. These improvements are indicated in the absorption spectra of Fig. 3(a).

Figure 2(d) depicts the field profile generated in the bare (non-metallic) architecture under TE-polarized illumination. Here also the field intensity in the volume of the active material is slightly stronger than the other layers. Figure 2(e) shows the electric field intensity behavior of the top grating architecture under TE-polarized illumination at $\lambda = 600$ nm. As observed in Fig. 3(b), the absorptivity performance is lower than that of the bare architecture. The field map demonstrates that the top metallic gratings reflect the incoming light, which decreases the optical absorption of the active material. Figure 2(f) presents the electric field profile for the bottom grating architecture. The change in Fabry-Perot resonance in absorbing material leads to strong field amplification because of introducing a nanopatterned metallic surface (bottom grating). The refractive index difference between the P3HT:PCBM (n ~1.45 at $\lambda = 600$ nm) and PEDOT:PSS (n ~2.1 at $\lambda = 600$ nm) layers causes total internal reflection, thus the light is trapped in the P3HT:PCBM active layer.
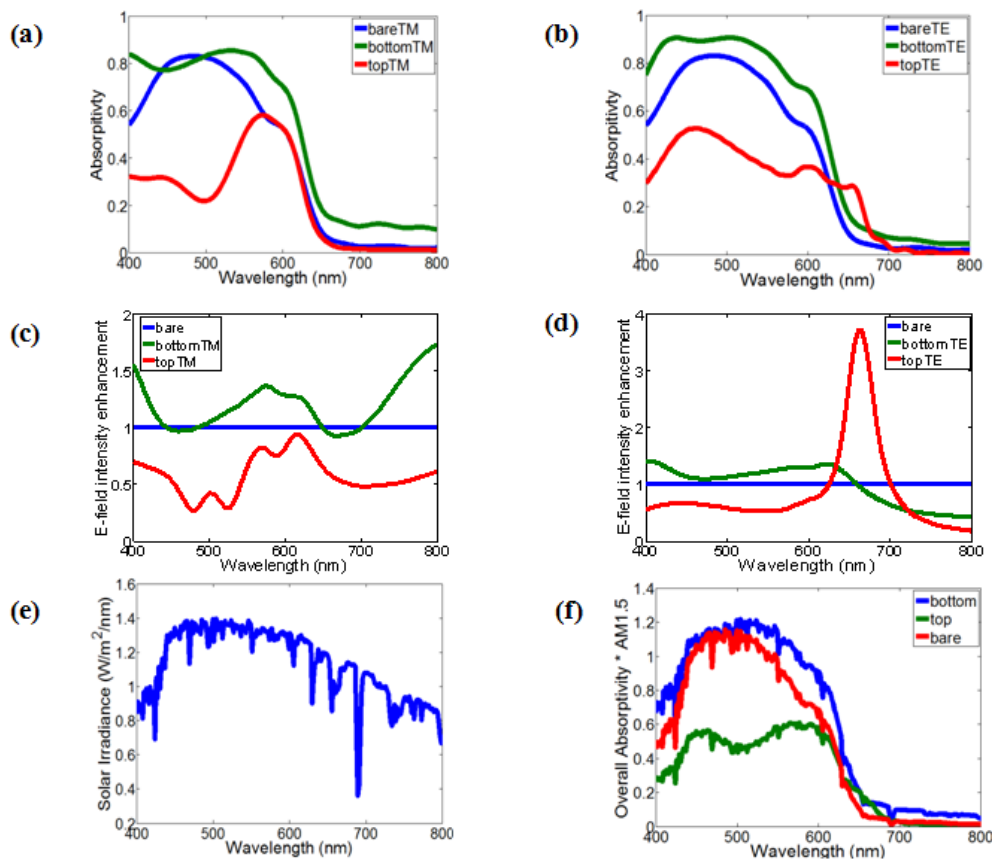

Fig. 3. Calculated absorption spectra of the organic active material in the bare, bottom grating, and top grating structures computed for the device parameter of P = 130 nm, LT1 = 150 nm, LT2 = 50 nm, LT3 = 100 nm, w1 = 50 nm, w2 = 50 nm, and h = 50 nm under (a) TM-polarized (Media 1) and (b) TE-polarized light illumination (Media 2). Electric field intensity enhancement within the volume of the organic active material using the bottom grating (given in Fig. 1(b)) and the top grating (given in Fig. 1(c)) structures compared to that generated in the bare structure, with this field enhancement shown for (c) TM-polarized and (d) TE-polarized light illumination. (e) Air mass (AM) 1.5G solar radiation. (f) Multiplication of AM1.5G solar radiation and overall absorptivity in the volume of the organic active material in the bare, bottom grating, and top grating structures.

Figure 3(c) and Fig. 3(d) present the electric field intensity (electric field square) enhancement in the volume of active layer in the bottom and top grating architectures in comparison to the electric field in the bare structure. Figure 3(c) shows that we enhance the electric field in the 400-800 nm region, except for small spectral ranges of 450-480 nm and 650-700 nm under TM-polarized illumination. In the 400-800 nm range, the electric field is boosted up to 1.7 folds by placing the bottom plasmonic structure. However, the top grating architecture reduces the electric field in the active material. This condition causes to decrease the overall absorption as observed in Fig. 3(a). Figure 3(d) shows that we enhance the electric field in the 400-650 nm region under TE-polarized illumination. In this range, the electric field is enhanced up to 1.4 folds with the bottom grating structure. The top grating architecture reduces the electric field intensity in the active material except for the enhancement in 630-700 nm range. In this range, the allowed waveguide modes at these frequencies leads to the localized surface plasmons located at the bottom of the top grating. The normalized field map of the top grating structure is given in Fig. 2(f). This field localization at these frequencies enhances the absorptivity in this wavelength range as shown in Fig. 3(b).
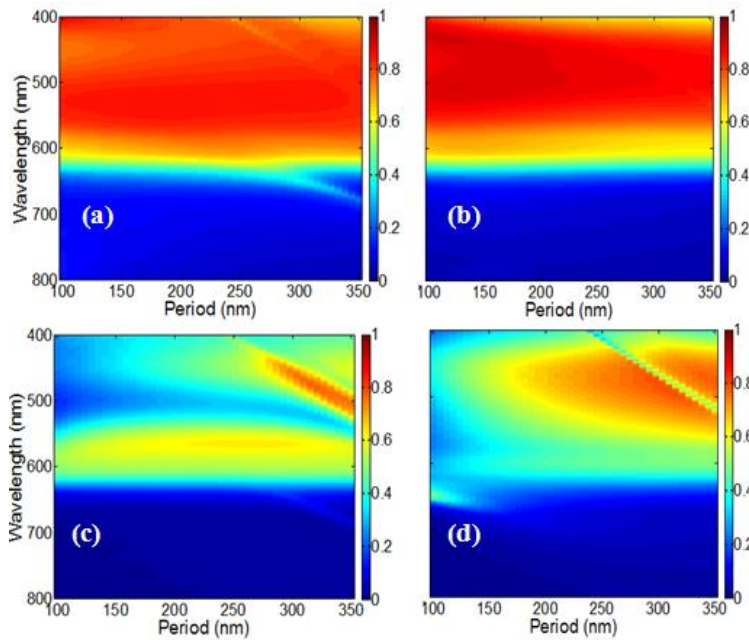

Fig. 4. Map of absorptivity in the active layer of (a) the bottom grating structure under TM, (b) the bottom grating structure under TE, (c) the top grating structure under TM and (d) the top grating structure under TE. The absorption spectra are shown for parameters of w1 = 50 nm, h1 = 50 nm, LT1 = 150 nm, LT2 = 50 nm and LT3 = 100 nm.

We also considered the effect of grating periodicity on the absorptivity under both TE- and TM-polarized illumination. The absorptivity *vs.* periodicity maps of the bottom grating structure under TM-polarized illumination, bottom grating structure under TE-polarized illumination, top grating structure under TM-polarized illumination and top grating structure under TE-polarized illumination are given in Fig. 4(a), Fig. 4(b), Fig. 4(c) and Fig. 4(d), respectively. All absorptivity *vs.* periodicity maps are normalized in the absorptivity range of 0-1. The absorptivity behavior of the bottom grating embedded architecture remains almost the same in the period range of 100-350 nm. For long periodicities, the absorptivity tends to decrease and match the absorptivity of the bare structure since the large field enhancement *via* excited surface plasmon modes per volume decreases and the plasmonic excitation behavior becomes insignificant. The top grating architecture has the lowest absorptivity behavior at every periodicity. For long periodicities, the absorption of active material in the top grating

architecture also increases since the top metallic grating stops reflecting and allows for more light to couple into the active material. Figure 5 presents the resulting multiplication of the overall absorption of $(A_{TM} + A_{TE})/2$ with AM1.5G solar spectrum.
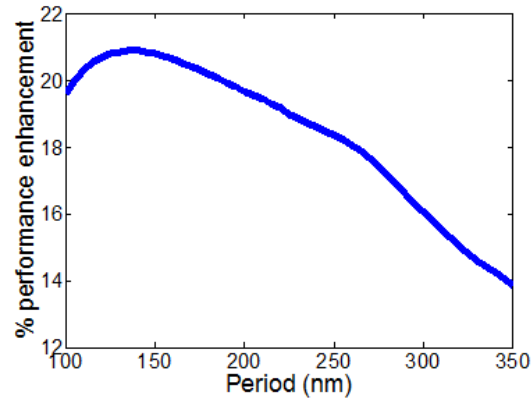

Fig. 5. Calculated absorption enhancement of plasmonic backside grating in comparison to the bare device computed for the following parameters: LT1 = 150 nm, LT2 = 50 nm, LT3 = 100 nm, w1 = 50 nm, and h = 50 nm.
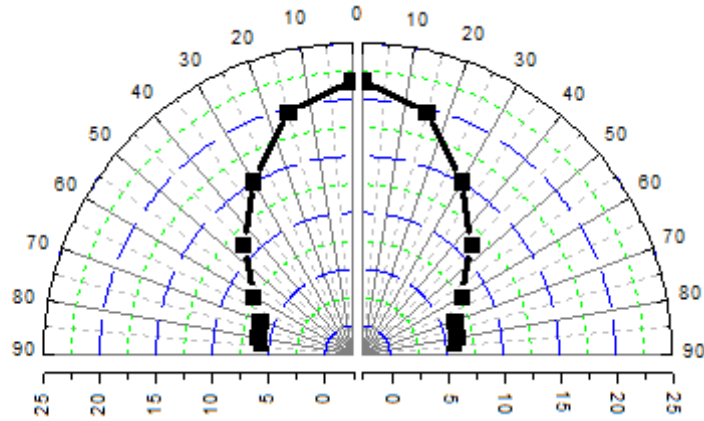

Fig. 6. Effect of the incidence angle on calculated overall total absorption enhancement in the plasmonic backcontact grating architecture. All device parameters are the same as those in Fig. 2.

The backcontact grating design exhibits improved enhancement levels compared to the top grating structure and the bare device for surface-normal configuration. In Fig. 6, we investigate how much the performance enhancement factor is reduced as the angle of incidence is increased from surface normal towards off-axis angles for the backcontact design. According to these simulations, the resulting absorption enhancement is relatively weak depending on the angle of incidence for the range of small angles in the case of the backcontact grating design. However, the optical absorption in the active layers further decreases with the increasing angle due to depleted localized SPRs around the metallic gratings. When the angle of incidence is increased, the light travels a longer way in the active material until it hits the metallic gratings on the backcontact surface. Thus, this reduces the intensity of the light, which results in weak surface plasmons and reduced field localizations around the metallic surfaces. We find out that the enhancement in the optical absorption of thin-film P3HT:PCBM drops to this half-maximum at an incidence angle of 45° compared to the same cell without a grating. The effect of incident angle on electric field distributions is depicted in Fig. 7 for large off-axis angles. In backcontact grating architecture, we do not add

any active material to compensate for the removed active material replaced by the metallic grating. However, the effect of removed active material becomes significant for large off-axis angles.
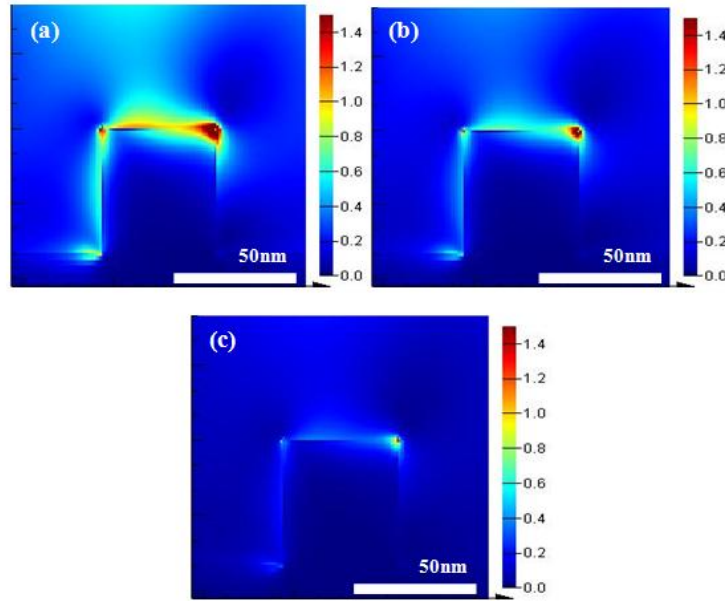

Fig. 7. Effect of the incidence angle on field distribution ($|E|^2$) in backcontact grating architecture at λ = 400 nm under TM-polarized illumination. Field distributions are given at illumination angles (a) 70°, (b) 75°, and (c) 80°. All device parameters are the same as those in Fig. 2.

4. Conclusion

In conclusion, we proposed and demonstrated numerically metallic grating backcontact structure that enables strong optical absorption in P3HT:PCBM based solar cells enhanced in all polarization for the first time. We modeled and simulated the performance of plasmonic architectures under both TE- and TM-polarized illumination and also presented the parametric study results for this device structure. By taking advantage of generated surface plasmon polaritons near metal/dielectric interface, we found out a plasmon assisted absorption increase up to ~21% in the active layers of this solar cell under TE- and TM-polarizations even when we effectively reduce the active material by replacing it with metallic gratings. The optical absorption enhancements occur in the most effective range of spectral distribution of sunlight (in 450-600 nm range). Plasmon enhanced absorption proposed in this work proves to be a promising approach to increase the performance of commonly used organic solar cells of P3HT:PCBM. This design strategy can potentially be extended to 3-dimensional metallic structures and different kinds of solar cell architectures.